UC Berkeley
UC Berkeley Electronic Theses and Dissertations

Title

A Theory of Nanoparticle Growth and a Theory of Thin Film Nucleation

Permalink

Author

Mastandrea, James P.

Publication Date

2017

Peer reviewed|Thesis/dissertation

A Theory of Nanoparticle Growth and a Theory of Thin Film Nucleation

by

James P. Mastandrea

A dissertation submitted in partial satisfaction of the

requirements for the degree of

Doctor of Philosophy

in

Engineering - Materials Science and Engineering

in the

Graduate Division

of the

University of California, Berkeley

Committee in charge:

Professor Daryl C. Chrzan, Chair
Professor Mark D. Asta
Professor Ali Javey

Spring 2017

A Theory of Nanoparticle Growth and a Theory of Thin Film Nucleation

Abstract

A Theory of Nanoparticle Growth and a Theory of Thin Film Nucleation

by

James P. Mastandrea

Doctor of Philosophy in Engineering - Materials Science and Engineering

University of California, Berkeley

Professor Daryl C. Chrzan, Chair

This dissertation is divided into two parts. The first will discuss a theory that was identified to narrow the size distribution of nanoparticles grown via ion beam synthesis (IBS). Specifically, a simple mathematical argument explains a processing route for the ion beam synthesis of nanoclusters with a narrowed size distribution. The key idea is that growth conditions for which the average nanocluster size is increasing rapidly can lead to narrowed size distributions. Modeling candidate processes using a self-consistent, mean-field theory shows that normalized nanocluster size distributions with full-width at half-maximum of 17% of the average can be attained.

The second part presents a theory for nucleation in confined high-aspect ratio thin films. Specifically, classical nucleation theory is used to consider the solidification of a melt confined between two planar surfaces. The critical nuclei shapes and the associated nucleation energy barriers are computed as a function of the thickness of the film, and the film's relevant bulk and interface energies. The analysis is then repeated for the melting transition, and expressions for the depression and elevation of the melting temperature are found. A nucleus morphology diagram is constructed. This diagram presents the lowest energy morphology of the nuclei, as well as melting points, as a function of the system parameters. Using the nucleus morphology diagram, experimental and system parameters that allow for the desired nucleation behavior can be identified. Furthermore, the nucleus morphology diagram illustrates a region of parameter space where the film is predicted to solidify above its thermodynamic bulk melting temperature, a behavior termed presolidification. The theory is used to predict the temperature at which nucleation of the solid phase and liquid phase are expected for Ge between two glass substrates. Furthermore, a possible route for controlling the orientation of the film is identified as confinement of the film can lead to a large range of solid phase nucleation temperatures, which are a function of the system's interfacial free energies. By controlling the growth temperature, certain orientations may not be able to nucleate thereby reducing the possible number of orientations within a film.

To my family.

Contents

List of Figures

List of Tables

Acknowledgments

First, I would like to thank my research advisor Prof. Daryl C. Chrzan for giving me the opportunity to work in his research group. For this I am incredibly grateful. Also, my sincerest thanks for your mentorship; I am a much better scientist and researcher because of this. I'd also like to express gratitude for your dedication to your students. From helping us develop tools to succeed professionally, to taking us on fun activities, my time in graduate school has been a very rewarding experience thanks to you.

Next, I would like to thank Prof. Joel Ager III, for his continual support in helping me with my research and for challenging me. This has improved the quality of my work and has made me a better researcher. I would like to acknowledge Prof. Eugene Haller and Prof. Ali Javey for allowing me to work in their labs and for teaching me many concepts through our fruitful scientific discussions. I would also like to thank Prof. Mark Asta, for being the chair of my qualification committee and for being on my dissertation committee. Our discussions about my research were very helpful and improved the quality of my research.

There are many students who helped me during graduate school. From Prof. Haller's group I would like to thank Karen Bustillo and Julian Guzman for our nanoparticle work. From Prof. Javey's group I would like to thank Kevin Chen and Rehan Kapadia for our collaboration on the thin film work. I would like to thank all of the students in Prof. Chrzan's group, specifically Cosima Boswell-Koller, Carolyn Sawyer, and Matthew Sherburne for their help in the nanoparticle work. I would also like to thank Yuzhi Zhou, Ian Winter, and Max Poschmann for their lab camaraderie and for our educational discussions.

Finally, I would like to thank my family. I'd like to thanks my parents for their support and commitment to their children. You two are my biggest role models and I want to thank you for everything you have done for me. I'd also like to thank my brothers Thomas and Nicholas for their support and encouragement to pursue my goals.

Chapter 1

Introduction

Understanding the growth of materials is central to materials science and engineering. This is due to the fact that a material's functional properties are directly linked to its structure, and the structure of a material is often dictated by its growth process. Consequently, insufficient knowledge of the growth behavior of a system can impede the creation of a material with promising behavior and the ability to produce it in a repeatable fashion. This dissertation is focused on modeling growth.

The work contained in this dissertation seeks to understand aspects of the growth behavior of two material systems: nanoparticles in a matrix and confined high-aspect ratio thin films. The emphasis is placed on developing theories able to optimize growth outcomes. The first part of this dissertation focuses on narrowing the size distribution of nanoparticles grown using a solid state technique: ion beam synthesis (IBS). The growth process entails implanting an insoluble atomic species into a matrix. These implanted ions then form clusters. As the properties of nanoparticles are typically size dependent, in order to create a functional device out of these material systems, a narrow nanoparticle size distribution is desired. In Chapter 2, a more thorough introduction into IBS is given along, and a theory to narrow the size distribution of nanoparticles is presented.

The second part of this dissertation presents a theory that focuses on nucleation of the melting and solidification transitions of a one component system in confined volumes. The specific geometry under consideration is confined high-aspect ratio thin films. Here, the film is confined in the sense that homogeneous nucleation behavior cannot occur. In Chapter 3, details of the theory used to model the nucleation process are presented along with how the melting temperature and nucleation behavior might be affected for this system under these constraints.

Chapter 2

Size Distribution Narrowing of Nanoparticles

2.1 Introduction

Nanocrystals are expected to have size dependent thermodynamic, electronic [1], and optical [2], properties. Accordingly, there is interest in generating nanocrystals of particular sizes in well defined positions in order to study and exploit the expected novel properties.

Chemists, by the means of colloidal chemistry, have had success in controlling the size and size distributions of nanocrystals [3, 4]. By varying growth conditions, nanoclusters with size distributions as narrow as 9 % of the average size have been synthesized [4]. These nanocrystals, however, remain in solution and are, most often, coated by an organic surfactant. Many applications require that these nanocrystals be embedded within another matrix, or arranged in an ordered pattern in order to exploit their unique properties. Though much progress has been made towards incorporating these nanocrystals into optoelectronic devices [5], there is still much work to be done.

Another approach is to synthesize the nanocrystals in place, using more traditional semiconductor processing routes. Towards this end, ion beam synthesis (IBS) is an attractive candidate for nanocrystal synthesis. During ion beam synthesis, ions are implanted into a matrix. The ions are chosen to be insoluble within the matrix material, and this results in precipitation of the ions into clusters, both during implantation and during the anneal that typically follows. The result is a collection of nanoscale sized precipitates embedded within a matrix.

IBS has several advantages. It is a very clean process that is compatible with modern semiconductor processing routes. Further, the mass of the implanted species can be controlled so that one can implant isotopically pure elemental species. One can also control the position of the ions, and hence the positions of the nanocrystals. Indeed, low-energy ion beam synthesis has been used to create nanocrystals for the exploration of novel modern memory devices [6].

However, the nanocrystal size distributions produced by typical, steady-state IBS are very broad. The widths of the size distributions often approach the average size of the nanocrystals [7]. Though there is some evidence that widths can be narrowed by implanting at a reduced temperature during a steady state implant (i.e. constant temperature, constant flux), this narrowing appears only capable of generating a distribution with widths of the order 1/2 the average size [8].

A number of groups have studied routes using ion implantation to control size distributions. Zhou *et al.* irradiated a thin film of Au on sapphire with Ar. This process produced Au nanocrystals embedded in sapphire with an average diameter of 3.9 nm and a standard deviation of 0.5 nm [9]. We estimate that the full width at half maximum from their narrowest published distribution is 14% - representing a very narrow distribution. However, this peak rests on a much broader background, and an analysis of the statistical significance of their results was not presented. Ramjauny *et al.* use ions to postprocess embedded nanocrystals that had been fabricated chemically [10]. The postprocessing is shown to convert the unimodal distribution into a bimodal one, and the distribution widths increase relative to the average size. Ramaswamy *et al.* perform a two stage implant of Au into SiO_2 wherein the first implant (dose 5×10^{14} cm^{-2}) is followed by a brief anneal meant to nucleate clusters that are then grown through a second implant (dose 1×10^{15} cm^{-2}). They obtain a distribution width of $\sim 40\%$, though again, a statistical analysis of their data is not presented [11].

Recently, however, an alternate processing route for narrowing size distributions during ion beam synthesis was identified using kinetic Monte Carlo simulations [12]. In the proposed process, one no longer conducts IBS using steady-state conditions. Instead, the temperature during implant is ramped from low to high. The distributions obtained within kinetic Monte Carlo simulations conducted using this process were quite narrow, but the fundamental physics governing the process were not presented in detail.

Here, the physics of the narrowing process is explained via a simple mathematical analysis. The physics of narrowing is then explored within a deterministic self-consistent mean-field theory [13, 14]. These explorations suggest that nanocrystal size distributions with widths as narrow as 17% of the average size should be achievable under experimentally accessible IBS conditions.

The following, then, presents the theory underlying an IBS processing route with the potential to substantially narrow nancrystal size distributions. Section II presents the theory of cluster size distribution narrowing. Section III studies the narrowing within a self-consistent mean-field theory for IBS, section IV presents a discussion and concluding thoughts.

2.2   Theory of Cluster Size Distribution Narrowing

The self-consistent mean-field theory for IBS used here was presented in detail within references [8], [13], [14], and [15]. Here, a summary of the model and relevant results are presented in order to frame the discussion.

The dynamics of IBS are complicated, and there are a number of kinetic processes that appear to be relevant to the evolving cluster size distributions. First and foremost, atoms are deposited within the matrix at a rate F (with dimensions of volume^{-1} time^{-1}). The deposited atoms diffuse within the matrix with a (radiation damage enhanced) diffusivity D. When an atom encounters another atom, or a cluster of atoms, the two particles will bind together. In this manner, clusters nucleate and grow. Atoms are also thermally emitted from clusters with a characteristic time τ_s governing the emission from a cluster containing s atoms. These times are computed using the appropriate thermodynamic laws, and, in the absence of the radiation damage associated with IBS, enable the model to display coarsening behavior akin to that modeled by Marqusee and Ross [14, 16]. However, ion implantation has the potential to damage existing clusters. If the deposited atom is placed within an existing cluster, the cluster is fragmented into smaller clusters (including single atoms) characterized by an empirically deduced power-law size distribution.

The self-consistent mean-field rate theory describes the time evolution of the average volume density of clusters of size s, $\langle n_s \rangle$. More specifically, the following differential equations govern the evolution:

$$
\begin{aligned}
\frac{d \langle n_1 \rangle}{dt} \;=\;& F - 2\, D\, \sigma_1 \langle n_1 \rangle^2 - D \sum_{j>1} \sigma_j \langle n_j \rangle \langle n_1 \rangle + 2\, \frac{\langle n_2 \rangle}{\tau_2} \\
& + \sum_{j>2} \frac{\langle n_j \rangle}{\tau_j} + F\, \Omega \sum_{j>1} \langle n_j \rangle \, (j+1)\, K_1 (\alpha, j)
\end{aligned}
\tag{2.1}
$$

$$
\begin{aligned}
\frac{d \langle n_s \rangle}{dt} \;=\;& D\, \sigma_{s-1} \langle n_{s-1} \rangle \langle n_1 \rangle - D\, \sigma_s \langle n_s \rangle \langle n_1 \rangle - \frac{\langle n_s \rangle}{\tau_s} \\
& + \frac{\langle n_{s+1} \rangle}{\tau_{s+1}} - F \langle n_s \rangle \, \Omega \, (s+1) \\
& + F\, \Omega \sum_{j>s} \langle n_j \rangle \, (j+1)\, K_s (\alpha, j).
\end{aligned}
\tag{2.2}
$$

Here, $K_s (\alpha, j)$ is the kernel indicating the number of clusters of size s produced from an ion directly impacting a cluster of j atoms, and α is the exponent characterizing the power-law fragment distribution. Ω is the atomic volume of the implanted species. The σ_s's are the capture lengths describing the attachment of a diffusing atom to a cluster containing s atoms. These capture lengths are determined self-consistently, as described in detail by Yi $et\ al$ [14]. Effectively, the capture length for a cluster of s atoms is found by solving a diffusion problem for the cluster in question. More specifically, a diffusing atom is less likely to attach to the cluster in question because it can be absorbed by another cluster. This absorption process is modeled as a uniform (in space) sink for diffusing atoms with a sink strength determined by the existing cluster size distribution.

This theory provides much insight into the steady-state IBS process. Under conditions of a steady-state implantation temperature and F, the cluster size distribution approaches a

steady-state shape, similar to the behavior displayed during coarsening. This shape, however, is most often more broad than the distribution expected from typical coarsening processes, with the width of the distribution approaching the average size [7].

During steady-state IBS, the average cluster size also approaches a constant in the long time limit. This is in contrast to coarsening, wherein the average cluster size continues to grow. During IBS, the probability that a cluster will be damaged, and thereby reduced in size, by an incoming ion increases with cluster size. Thus ion beam damage counteracts the effects of coarsening to produce a characteristic size.

Despite the apparent steady-state cluster size distribution, the individual clusters are evolving in time. It is convenient to focus on the radius of the cluster, R, rather than on the number of atoms within the cluster, s, when considering this evolution, as this enables one to make direct connections with the extensive literature on size focusing during chemical synthesis of nanoparticles. Let $P(R,t)\,dR$ be the probability that a nanocrystal selected at random from all the nanocrystals has a radius between R and $R+dR$ at time t. The (time-dependent) average radius, $\langle R \rangle$ is defined according to

$$\langle R \rangle = \int_0^\infty R\,P(R,t)\,dR. \tag{2.3}$$

In the case of traditional coarsening, it is often true that the while $\langle R \rangle$ continues to change in time, the shape of the distribution $P(R,t)$ attains a steady state form [17]. This steady state form can be revealed by plotting the scaled size distributions $P(\rho) \equiv \langle R \rangle P(R,t)$ as a function of $\rho \equiv R/\langle R \rangle$. Plotting distributions in this fashion allows one to assess the width of the distribution independently of its average size, and thereby enables one to meaningfully compare the widths of distributions with different average sizes.

Insight into the evolution of the cluster size distribution can be gleaned from examination of the time derivative of ρ, $d\rho/dt$, as a function of ρ (Fig. 2.1). Ratke and Voorhees present a description of the size distribution evolution expected from these different types of curves, and their discussion is summarized here [17]. Consider, then, the width of the scaled size distribution. The evolution of this scaled distribution is determined by the dynamics of the evolving clusters. These dynamics are captured, in part, by the quantity $d\rho/dt$. Under typical coarsening conditions, the dependence of $d\rho/dt$ on ρ is that shown in Fig. 2.1(a). As Ratke and Voorhees note, *all* clusters characterized by $\rho < \rho_{\max}$ shrink relative to the average size. The result is a distribution in which the absolute width increases in time, though the width relative to the average size approaches a constant. Figure 2.1(b) displays a hypothetical situation in which $d\rho/dt$ is positive for $\rho_1 < \rho < \rho_2$, and negative elsewhere. Should the dynamics of cluster evolution be governed by such a law, the ultimate distribution would be monodisperse with size $\rho = \rho_2$. Clusters with $\rho < \rho_1$ would shrink until they disappeared. Clusters with $\rho_1 < \rho < \rho_2$ would grow until they reached a size such that $\rho = \rho_2$. Similarly, clusters initially described by $\rho > \rho_2$ would shrink until $\rho = \rho_2$. In the end, *all* clusters would be characterized by $\rho = \rho_2 = 1$.

While the case of Fig. 2.1(b) does not apply to coarsening, it does suggest a route to narrowing cluster size distributions using IBS. Consider the following derivative:
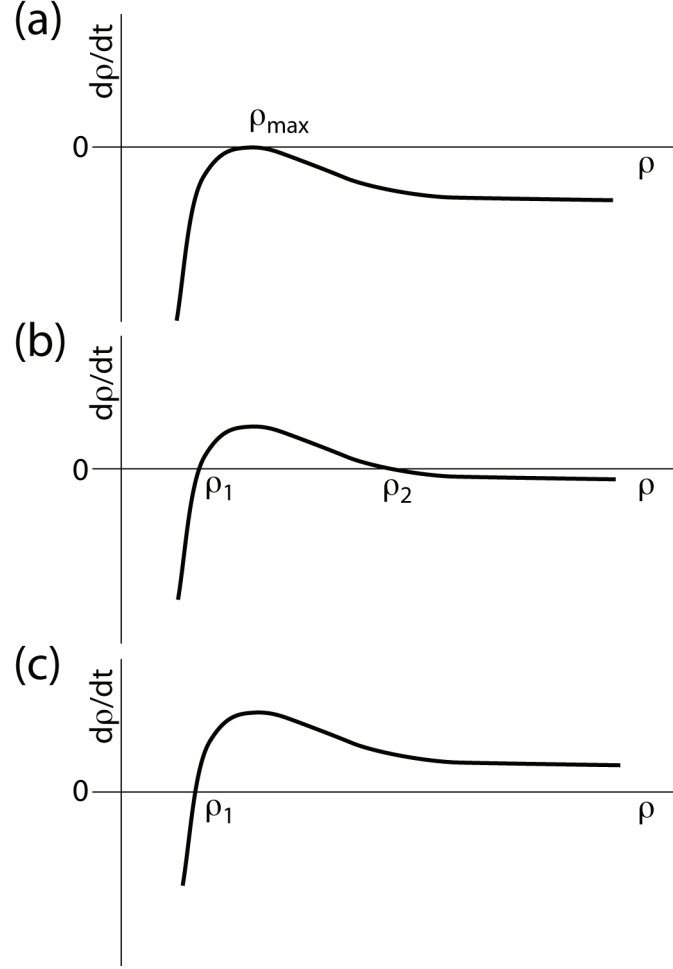
Figure 2.1: (a) A sketch of $d\rho/dt$ for the typical coarsening case. All those clusters with a scaled radius below ρ_{max} shrink relative to the maximum cluster. There are no clusters larger than ρ_{max} within the distribution. (b) A schematic describing the dynamics of a hypothetical growth process. Clusters with $\rho < \rho_1$ will shrink relative to the average size, and will eventually vanish. Clusters with $\rho_1 < \rho < \rho_2$ will grow more rapidly than the average until they reach the value ρ_2. Clusters with $\rho > \rho_2$ will shrink also until they reach the value ρ_2. (c) Sketch of typical behavior for $d\rho/dt$ observed during steady-state IBS, absent the influence of ion beam damage. All clusters larger than ρ_1 grow faster than the averaged size cluster, and all clusters smaller that ρ_1 shrink relative to the average size.

$$
\begin{aligned}
\frac{d\rho}{dt} &= \frac{d}{dt}\frac{R}{\langle R \rangle} \\
&= \frac{1}{\langle R \rangle}\frac{dR}{dt} - \frac{R}{\langle R \rangle^2}\frac{d\langle R \rangle}{dt}.
\end{aligned} \tag{2.4}
$$

Eq. (2.4) makes clear the approach to size distribution narrowing. In the steady-state IBS process, $\langle R \rangle$ approaches a time independent value, the second term on the right is identically zero, and $d\rho/dt$ is proportional to dR/dt. Figure 2.1(c) shows the typical behavior of $d\rho/dt$ in the steady-state regime obtained from the self-consistent mean-field theory, absent the influence of ion beam damage to existing clusters(see below). Note that $d\rho/dt$ crosses $d\rho/dt = 0$ only once, and is positive for larger values of ρ. The dynamics suggested by such a curve would have the clusters growing indefinitely. As noted above, the effects of ion beam damage counteract this tendency and leads to the statistically steady state.

Suppose, now, that the growth conditions could be changed so that the average radius of the clusters is increasing (*i.e.* $d\langle R \rangle/dt > 0$). During this period, the second term on the right hand side of Eq. (2.4) becomes negative. Moreover, this term is weighted by the radius of the clusters, suggesting that it will be more negative for larger clusters. Given these properties, the non-steady state conditions have the potential to convert the $d\rho/dt$ curve into one with the form shown in Fig. 2.1(b). As noted above, if the clusters are governed by this growth law, the size distribution will begin to narrow.

This observation is the key to designing IBS processing routes leading to narrower size distributions: one simply needs to design growth conditions to transition between two statistically steady state situations characterized by different values of the the mean radius such that $\langle R \rangle_{\text{initial}} < \langle R \rangle_{\text{final}}$. During the transition between the two statistically steady states, there will be a tendency for the size distributions to narrow. This very general result can be applied to the narrowing of cluster size distributions using IBS.

2.3   Narrowing Within a Self-Consistent Mean-Field Theory for IBS

Consider a typical IBS experiment. From Sharp *et al.* [7], the thickness of the implanted layer is approximately 100 nm. Thus, a 4.11 x 10^{16} cm^{-2} dose corresponds to a volumetric dose of 4.11 x 10^{-3} Å^{-3}; however, the area based dose will be used as the standard throughout this dissertation when explaining a simulation's design. Furthermore the implantation will be completed over 8 hours, and therefore the flux used is 1.43 x 10^{-7} Å^{-3} s^{-1}. The main parameters for the simulation are the following and were chosen to represent Ge atoms in a amorphous SiO$_2$ matrix. Arrhenius equations are used to model the diffusion and solubility. For diffusion, 4.2 x 10^{13} Å^2 s^{-1} is the prefactor [15], and 0.4 eV is the activation energy [12]; and for the solubility, 0.0047 Å^{-3} is the prefactor [12, 14], and the activation energy is 0.816 eV [12]. The atomic volume of Ge is 22.7 Å^3. For this work, the energy of the cluster/matrix interface was set to 0.6 J m^{-2}, which is smaller than the expected cluster/matrix interface energy for Ge [13], but using larger, more accurate values makes the computation more expensive, while not altering the final trends of the implant. As used by Yuan *et al.* [8], the power law coefficient used to model the fragmentation is 2.3 [18].
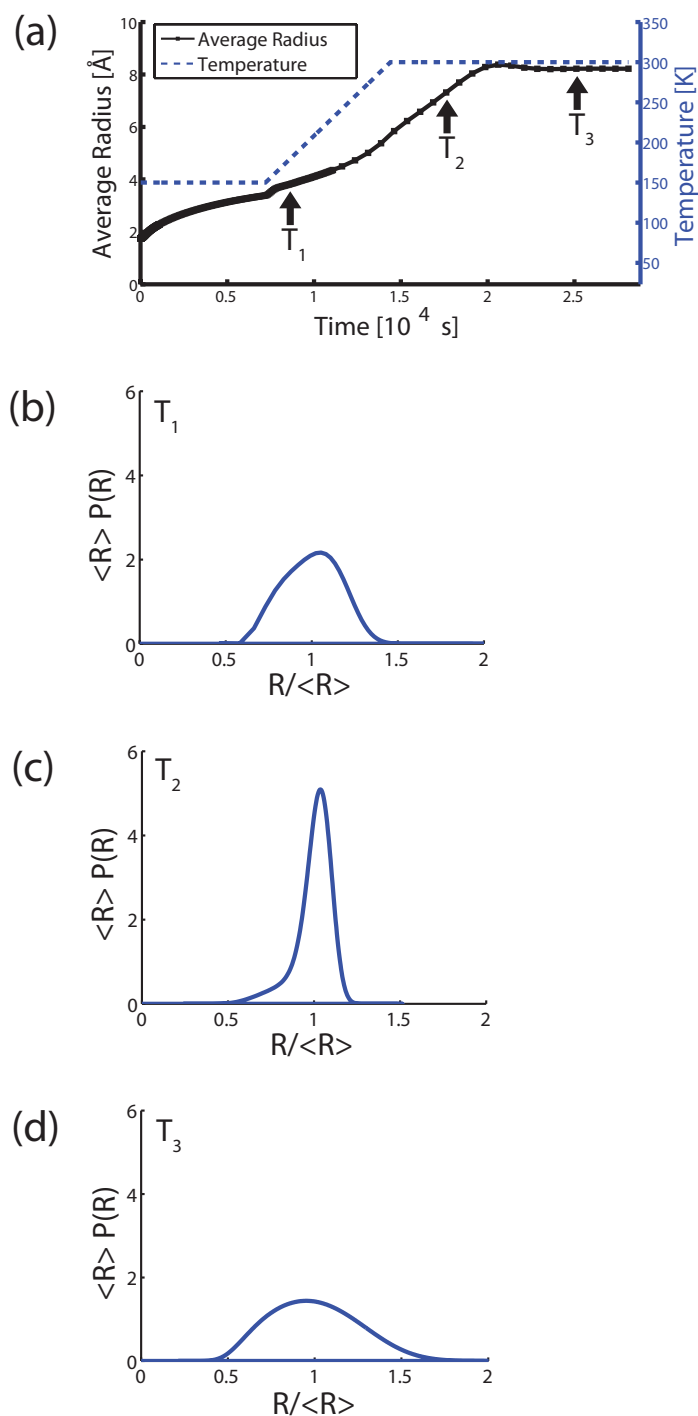
Figure 2.2: (a) Average radius and temperature profile versus implant time, during a non-steady state IBS experiment, where the system transitioned from a steady state system defined by 150 K, to a steady state system defined by 300 K. (b) Scaled nanocluster size distribution at time T_1, 8.61 x 10^3 s. (c) Scaled nanocluster size distribution at time T_2, 1.76 x 10^4 s. (d) Scaled nanocluster size distribution at time T_3, 2.51 x 10^4 s.

Now consider the following non-steady state IBS experiment. Set the initial temperature to 150 K, and implant 1.03 x 10^{16} atoms cm^{-2} over the course of 2 hours. Then for the following 2 hours, implant another 1.03 x 10^{16} atoms cm^{-2} while linearly ramping the temperature from 150 K to 300 K. Once that has been completed, implant 2.06 x 10^{16} atoms cm^{-2} at a fixed 300 K for 4 hours. The evolution of the average radius versus implantation time, along with the temperature profile as a function of time, is shown in Fig. 2.2(a).

While the system is kept at a constant temperature of 150 K, the average radius of the clusters approaches a constant value termed the steady state average radius (SSAR). The cluster size distribution is relatively broad. At a time shortly before T_1, the temperature begins ramping at a fixed rate, but the size distribution remains relatively broad, Fig. 2.2(b). Between times T_1 and T_2, the size distribution narrows, ultimately reaching a full-width at half maximum of 17 % of the average radius, Fig. 2.2(c). By the time T_3, the size distribution and SSAR associated with the new conditions are established, Fig. 2.2(d).

This behavior can be rationalized empirically using eq. (2.4). However, we can gain further insight by examining the self-consistent mean-field theory. Begin by considering the dynamics in the absence of fragmentation. In this limit, we can compute the $d\rho/dt$. Following Yi et $al.$ [14], one can write:

$$\frac{ds}{dt} = D\langle n_1 \rangle \sigma(s) - \frac{1}{\tau(s)} \tag{2.5}$$

$$R(s) = \left(\frac{3\Omega}{4\pi} s \right)^{1/3}. \tag{2.6}$$

In eq. (2.5), D is the diffusion coefficient for a monomer, $\langle n_1 \rangle$ is the average concentration of monomers, σ is the capture length of a given cluster, and $1/\tau(s)$ is the rate at which atoms desorb from a given cluster of size s. Ω in eq. (2.6) represents the atomic volume of a monomer, which in this example is taken to be the atomic volume of a single Ge atom. Differentiating eq. (2.6) with respect to time yields the expression for dR/dt.

$$\frac{dR}{dt} = \left(\frac{3\Omega}{4\pi} \right)^{1/3} \frac{\frac{ds}{dt}}{3s^{2/3}} \tag{2.7}$$

Substituting eq. (2.5) into eq. (2.7) allows $d\rho/dt$ to be computed, once $d\langle R \rangle/dt$ is known. $d\langle R \rangle/dt$ is calculated from the simulations using a finite difference approach, where n is the index representing the step in the numerical iteration.

$$\left(\frac{d\langle R \rangle}{dt} \right)_n = \frac{\langle R \rangle_{n+1} - \langle R \rangle_{n-1}}{t_{n+1} - t_{n-1}} \tag{2.8}$$

However eq. (2.8) does take into account fragmentation, since it uses the average radius of the system as a function of time. Furthermore, although eq. 2.5 does not include terms for fragmentation, it is affected by fragmentation since fragmentation influences the average

concentration of monomers, $\langle n_1 \rangle$. Consequently, the values of $d\rho/dt$ in Fig. 2.3 will partially take fragmentation into account.
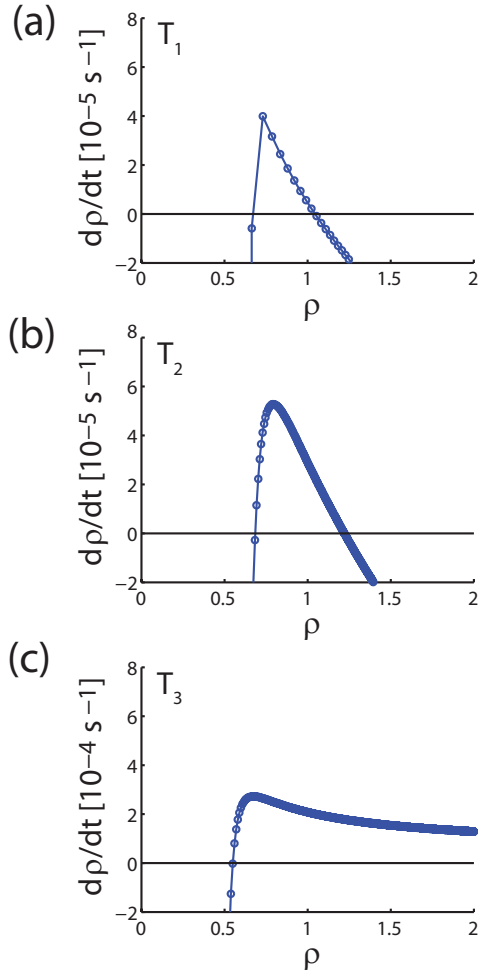
Figure 2.3: (a) $d\rho/dt$ as a function of ρ at time T_1, 8.61 x 10^3 s. (b) $d\rho/dt$ as a function of ρ at time T_2, 1.76 x 10^4 s. (c) $d\rho/dt$ as a function of ρ at time T_3, 2.51 x 10^4 s, please note the order of magnitude difference on the y - axis for this figure.

Using the same simulation as shown in Fig. 2.2, $d\rho/dt$ as a function of ρ is displayed in Fig. 2.3 at times T_1, T_2 and T_3. At time T_1, the temperature is being ramped. Consequently $d\langle R \rangle/dt$ is a non-zero positive number. When $d\langle R \rangle/dt$ is positive and significantly large, the right-term on the right side of eq. (2.4) subtracts from the left-term on the right side of eq. (2.4). At large values of ρ, this mathematical relation produces a second zero, as evident in Fig. 2.3(a). As discussed above, this dependence on ρ can lead to size focusing, particularly if it persists for an extended period of time. This dependence continues while the average radius of the system is increasing during the SSAR transition as seen in Fig.

2.3(b). However, as the system approaches the final SSAR, $d\rho/dt$ evolves to a state that only has one zero. This occurs because at T_3, $d\langle R\rangle/dt$ is approximately zero, thus the right term on the right side of eq. (2.4) is essentially zero. Figure 2.3(c) has the behavior of Fig. 1(c), and therefore no size focusing is present. These observations are the key details in determining why SSAR transitioning produces size narrowing of nanoparticles.

Note that the $d\rho/dt$ curves do not assume the form shown in Fig. 1(a). This is because under the influence of the ion flux, the steady state coarsening regime is never obtained. Although fragmentation was not fully taken into account for the Fig. 2.3 plots, it is presumed that the fragmentation wouldn't alter the general shape of the dρ/dt curves. The probability of a cluster being struck by a incoming ion is proportional to the cluster size (most of the impingement takes place at the end of range, so that the directionality of the implant is lost), and thus the larger clusters are preferentially fragmented. Thus it is expected that the only way fragmentation would change these curves would be by shifting the tail end of the dρ/dt curves down, and would have an increased effect as ρ increased. However, this effect would only increase the effectiveness of the growth conditions described by Fig. 2.3(a) and 2.3(b), and it is presumed that this would not shift the tail end of the curve down far enough to alter a growth situation described by Fig. 2.3(c).

2.4   Discussion and Conclusions

Equation (2.4) can serve as a guide for the optimization and development of growth cycles leading to narrower size distributions. Defining growth conditions so that the growth rate curves appear as in Fig. 1(b) is key to the process. Equation (2.4) suggests that this can be accomplished by ensuring that $d\langle R\rangle/dt$ is large and positive. One can then use intuition and an understanding of the growth process to develop processing routes.

An obvious first step is to increase $d\langle R\rangle/dt$ by increasing the final SSAR. This can be accomplished within the model by increasing the final temperature of the ramp. Figure 2.4 demonstrates the effects of temperature on the growth dynamics. The growth parameters are those governing the results in Fig. 2.2, henceforth referred to as case (C). Except for cases (A) and (B), the final temperatures have been reduced to 250 K and 275 K respectively. Since the cases have different final temperatures, the final SSARs are different. The time duration of the temperature ramps are the same for all three cases, but due to the different SSARs, $d\langle R\rangle/dt$ is different for each case.
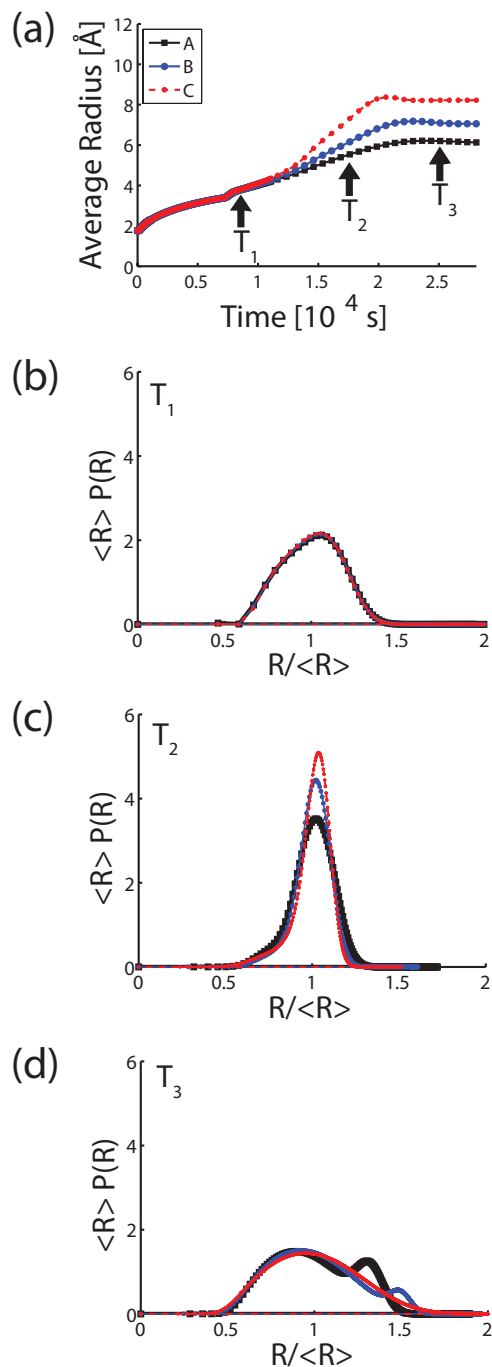
Figure 2.4: (a) A: Transition from a steady state system defined by 150 K and to a steady state system defined by 250 K. B: Transition from a steady state system defined by 150 K and to a steady state system defined by 275 K. C: Transition from a steady state system defined by 150 K and to a steady state system defined by 300 K. (b) Scaled nanocluster size distribution at time T_1, 8.61 x 10^3 s. (c) Scaled nanocluster size distribution at time T_2, 1.76 x 10^4 s. (d) Scaled nanocluster size distribution at time T_3, 2.51 x 10^4 s.

As seen in Fig. 2.4(a), case C had the greatest value of $d\langle R\rangle/dt$ during the SSAR transition, as expected. Figures 2.4(b), 2.4(c), 2.4(d), again show the behavior of the size distribution during the SSAR transition, and as evident from Fig. 2.4(c), the narrowest size distribution is produced by the SSAR transition that had the greatest value of $d\langle R\rangle/dt$.

The theory allows identification of additional processing routes leading to narrower size distributions. For instance, as the interface energy between the matrix and the nanocluster increases, the average size of the particles will become larger. Perhaps additions that alter the interface energy over time can be implanted, thereby leading to a positive $d\langle R\rangle/dt$. One might also increase the ramp rate, by reducing the time of the ramp. However, the system still needs time to adjust, so ramping using a step function versus the ramp times presented in this paper essentially does not alter the best size distribution the system can attain. The theory should enable one to identify growth conditions leading to narrower size distributions with a given average size.

There are limits on this process. For instance, the average cluster size one can produce must be larger than the smallest possible average cluster size obtainable by steady state IBS. Furthermore, IBS typically results in a nonuniform concentration of the implanted species. This, in turn, potentially translates into variation of the size distribution with position in the sample. The mean-field theory presented here, assumes a uniform implantation rate and composition. The key assumption in the theory is that the only sinks for atoms diffusing within the matrix are the clusters themselves. The edges of the implantation region serve as additional "sinks" in that atoms can effectively leave the system being modeled. If the distance between neighboring clusters is much less than the distance to the edges of the implanted region, the influence of the composition variation will not be significant. Images of implanted clusters confirm that the average separation between clusters is much less than the thickness of the implanted region, suggesting that the mean-field theory will be a reasonable approximation to the experimental system [11, 7].

It is interesting to compare the growth process suggested here with that presented by Ramaswamy *et al.* [11]. The strategy underlying their work is to separate the nucleation and growth phases of the synthesis. In this respect, the work mimics the approach used during chemical synthesis of nanocrystals [3]. An initial implant is performed, the sample is annealed at high temperature to complete the nucleation process, and then a second implant is performed at an elevated temperature to reduce nucleation and enable growth. Ideally, this results in a narrow size distribution for the clusters. In fact, Ramaswamy *et al.* present a size distribution with a width of approximately 40% the average size.

This approach, however, must be executed with care and may not be applicable in all situations. In their analysis, Ramaswamy *et al.* ignore the damage to existing clusters induced by the implantation during the growth stage. While this may be appropriate for their studied system, it is not be appropriate for all others, particularly those systems for which the implantation dose is necessarily high (such as the conditions used in reference 10). Under high dose conditions, the implantation during the growth phase ultimately fragments the growing clusters, and destroys the initial distribution of nuclei. The distribution resulting for the two stage implant, then, would be what one expects from steady state IBS at the

growth temperature. In contrast, the processing route described here fully accounts for ion beam damage to the growing clusters, and suggests that narrowing is possible even if ion beam damage is present.

Chapter 3

Nucleation of Melting and Solidification in Confined High Aspect Ratio Thin Films

3.1 Introduction

Thin film growth using standard methods typically leads to grain sizes on the order of or smaller than the film thickness. However, for many applications, such as opto-electronics and photovoltaic thin films, larger grain sizes are desired. Accordingly, recent developments in thin film growth techniques have been aimed at the growth of polycrystalline thin films, with large grains in comparison to the film's thickness. For example, S. Hu *et al.* [19], have demonstrated the growth of 30 μm by 30 μm single crystal Ge islands using Ge nanowires as seeds, with film thicknesses ranging from 30 nm to 1 μm. In their process, Ge nanowires are grown vertically from a Si substrate and are then encapsulated by SiO_2. After polishing the top surface, amorphous Ge and SiO_2 are deposited such that the amorphous Ge is encapsulated by SiO_2 and in contact with a Ge nanowire. Using the liquid phase epitaxy growth technique, the sample then underwent a rapid thermal anneal to a temperature above the melting temperature of Ge, and the authors state that they believe the Ge became a liquid. Solid Ge, seeded by the Ge nanowire, then grew and created a single crystal Ge island. This process demonstrated the ability to grow single crystal high aspect ratio thin films on a non-epitaxial surface using an epitaxial seed.

R. Kapadia *et al.* [20] developed the thin-fim vapor-liquid-solid (TF-VLS) growth technique and produced polycrystalline InP thin films with grain sizes ranging from 10 μm to 100 μm with an approximate film thickness of 3 μm, on a non-epitaxial surface without directly seeding the nucleation process. The films were created by depositing In on a polished Mo foil, and then capping the In with a SiO_x layer. The system was then annealed in a P environment, above the melting temperature of In, such that the In became a liquid. Phosphorous diffused through the SiO_x layer, mixed with the In liquid, and InP nucleated

and grew from the liquid solution. Further work on this process yielded the ability to control the nucleation sites by patterning MoO_x on the Mo foil, where nucleation preferentially occurred on the MoO_x [21]. Using this concept, K. Chen *et al.* [22], developed the templated liquid-phase crystal growth (TLPCG) technique. In this work MoO_x-In-SiO_x stacks are lithographically patterned on the surface of glass or Si/SiO_2 substrates, and then are encapsulated by SiO_x. Subsequent annealing above the melting temperature of In in a P environment yielded InP thin films in the templated geometry. Furthermore, growth and geometric conditions were found that produced twinned single crystal InP thin films in a cylindrical shape with diameters up to 7 μm.

A key factor in growing large grained thin films is the ability to control nucleation. Typically thin films with large grains are desired. Given that the final as-grown microstructure is closely related with the nucleation process, fewer nuclei will typically increase the as-grown grain sizes of the film. Thus a detailed understanding of the nucleation process may help to improve upon these growth techniques. Furthermore, as new technology tends to favor smaller components, the ability to predict nucleation in confined high aspect ratio thin films is of greater importance.

One expects TF-VLS and TLPCG to be dominated by heterogeneous nucleation: nuclei within the confined film form on an interface. In order to form a stable nucleus, a critical size of a cluster of atoms/molecules needs to be achieved. As the thickness of the film is decreased a fundamental question arises: what happens to the nucleation process as the thickness of the thin film becomes comparable to, or even less than, the dimension of the critical nuclei?

In order to address this question, the nucleation of the solid phase from a single component melt confined between two planar solid substrates is modeled using classical nucleation theory. While this model is not directly applicable to TF-VLS and TLPCG methods, it provides insight into the effects of confinement on nucleation. This simple model can form the basis for models of increased complexity. Using an isotropic interface energy model, and assuming that the volumetric change between the solid and liquid phase is negligible, critical nucleation energy barriers are determined as a function of the film's thickness and the film's interface and bulk free energy parameters. Two nucleus geometries are considered. Heterogeneous nuclei within an isotropic interface energy model have the geometry of a spherical cap, a geometry hereafter referred to as cap nucleation. The other geometry considered is when the critical nucleus grows in contact with both the top and bottom substrate and is called a catenoid-like (CL) nucleation (catenoid-like because it is not a true catenary).

Using the critical nucleation energy barriers calculated for cap and CL mediated nucleation, a nucleus morphology diagram (NMD) is created. This diagram illustrates which nucleation type has the lowest critical nucleation energy barrier, as well as displaying shifts in melting points relative to the thermodynamic bulk melting temperature, as a function of the system's interfacial and bulk energy values, and the thickness of the film. When constructing the NMD, cap nucleation is only considered, due to a physical constraint, when the height of the critical cap nucleus, h_c^{Cap} is less or equal to the height of the film, H. When $h_c^{Cap} > H$, only CL nucleation is considered. The geometry of the two different nuclei types

is illustrated in fig. 3.1, which also defines the contact angles made between the top and bottom substrate and the nuclei where applicable.
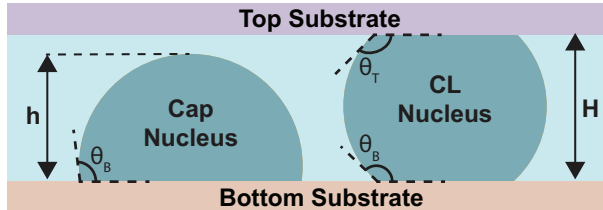
Figure 3.1: Cross sectional illustration of the system's geometry for the cap and CL nucleation types. θ_i is the contact angle between the nucleus and the top (T) or bottom (B) substrate.

The nucleation and growth, along with the melting and solidification behavior of thin films has been studied for unconfined [23, 24] and confined [25, 26] thin film systems. In 1986, Takagi [25] derived a theoretical relation for the change in the transition temperature from one phase to another in a confined thin film as a function of the film's thickness and the film's bulk and interface energy values, and used that theory to calculate a depression of the melting temperature for Pb and Au. Expressions presented in this dissertation are in agreement with the theoretical relation found by Takagi [25]. These expressions are expanded to explore the implications of situations not discussed by Takagi, such as how the transition temperature changes when the top and bottom substrate are not the same. Additionally, to the best knowledge of the author there has been no systematic study of barriers to nucleation.

In the next section, a dimensionless version of a rudimentary classical nucleation theory is presented. In the results section, first a slice of the NMD is presented illustrating the nucleation behavior for the symmetric case, where the top and bottom substrate are the same. Then the full NMD is shown, illustrating the nucleation behavior when the top and bottom substrate are not necessarily the same. Next, relations for the depression and elevation of the film's melting temperature are shown. In the discussion section the theory will be extended to the melting phase transition, and applications of the theory, limits of the theory, and future work will be presented.

3.2   Dimensionless Classical Nucleation Theory

From classical nucleation theory [27, 28] it is known that for homogeneous nucleation, the critical radius, r_c, and critical nucleation energy barrier, ΔG_c^{Hom}, are

$$r_c = \frac{2\gamma_{S,L}}{\Delta G_v}, \tag{3.1}$$

$$\Delta G_c^{Hom} = \frac{16\pi(\gamma_{S,L})^3}{3(\Delta G_v)^2}, \tag{3.2}$$

where $\gamma_{S,L}$ is the interface energy of the solid-liquid interface and for solidification ΔG_v is the difference between the Gibbs free energy of the liquid phase from the solid phase per unit volume: $\Delta G_v = G_v^L - G_v^S$, with G_v^L (G_v^S) the free energy per volume of the liquid (solid) phase. In order to express ΔG_v in terms of material parameters and the temperature, it will be approximated as

$$\Delta G_v \simeq \frac{\Delta H_v^F \Delta T}{T_M}, \tag{3.3}$$

where ΔH_v^F is the latent heat of fusion per unit volume, $\Delta T = T_M - T$, and T_M is the thermodynamic bulk melting temperature.

For cap nucleation the critical radius is the same as that for homogeneous nucleation and

$$\Delta G_c^{Cap} = \Delta G_c^{Hom} S(\theta), \tag{3.4}$$

where $S(\theta)$ is a shape factor, and θ is the contact angle between the nucleus and the substrate (fig. 3.1):

$$S(\theta) = \frac{(2 + cos(\theta))(1 - cos(\theta))^2}{4}. \tag{3.5}$$

The free energy change associated with the creation of a CL nucleus is

$$\Delta G^{CL} = -V_S \Delta G_v + A_{S,L} \gamma_{S,L} + A_B \Delta \gamma_{S-L,B} + A_T \Delta \gamma_{S-L,T}, \tag{3.6}$$

with A_B and A_T the contact areas between the bottom (B) and top (T) substrate respectively, and $\Delta \gamma_{S-L,i} = \gamma_{S,i} - \gamma_{L,i}$, where $i = \{B, T\}$, and $\gamma_{S,i}$ and $\gamma_{L,i}$ are the interface energy terms between the solid and liquid with substrate i respectfully. Determining the critical value of ΔG^{CL} for a specific system is not as trivial as solving for ΔG^{Hom} and ΔG^{Cap}. For a given set of the system's interface and bulk energy values and the thickness of the film, the shape of the nucleus at its critical size needs to be determined in order to find ΔG_c^{CL}. To calculate this, the calculus of variations is used [29]. However, in order to make the problem more tractable, a characteristic length and energy are chosen to nondimensionalize the problem. The characteristic length is chosen to be the critical radius, eqn. (3.1), and the characteristic energy is $\gamma_{S,L} r_c^2$. This reduces the number of material parameters in ΔG_c^{Cap}, ΔG_c^{Hom}, and ΔG^{CL} by two.

A consequence of using the critical radius as the models length scale is noted. As evident by eqn. (3.1) and eqn. (3.3), when $T > T_M$ or $T < T_M$ the length scale is a finite value and the model is valid, within the limits of the approximations made by the model. However, when $T = T_M$, the model's length scale diverges. When $T > T_M$, the length scale is negative; however, the length scale can formally be treated as positive by changing the sign of ΔG_v in eqn. (3.6), such that the $V_S \Delta G_v$ term increases the free energy of ΔG^{CL} when $T > T_M$.

Nondimensional quantities, indicated by a tilde, are defined as follows:

$$\widetilde{\Delta G_i^j} = \frac{\Delta G_i^j}{\gamma_{S,L} r_c^2}, \tag{3.7}$$

$$\widetilde{V_S} = \frac{V_S}{r_c^3}, \tag{3.8}$$

$$\widetilde{\Delta G_v} = \frac{\Delta G_v r_c}{\gamma_{S,L}}, \tag{3.9}$$

$$\widetilde{A_i} = \frac{A_i}{r_c^2}, \tag{3.10}$$

$$\widetilde{\gamma_{i,j}} = \frac{\gamma_{i,j}}{\gamma_{S,L}}, \tag{3.11}$$

$$\widetilde{\Delta \gamma_{i-j,k}} = \frac{\Delta \gamma_{i-j,k}}{\gamma_{S,L}}. \tag{3.12}$$

Applying these expressions to ΔG_c^{Hom} and ΔG_c^{Cap} yield their dimensionless analogs:

$$\widetilde{\Delta G_c^{Hom}} = \frac{4\pi}{3}, \tag{3.13}$$

$$\widetilde{\Delta G_c^{Cap}} = \widetilde{\Delta G_c^{Hom}} S(\theta). \tag{3.14}$$

In order to determine where in parameter space cap nucleation is possible, the nondimensionalized height for cap nucleation is, $\widetilde{h_c^{Cap}} = 1 - cos(\theta)$. (For reference, $\widetilde{h_c^{Hom}} = 2$ for homogeneous nucleation.)

Using equations (3.7) through (3.12), ΔG^{CL} in dimensionless form becomes,

$$\widetilde{\Delta G^{CL}} = -\widetilde{V_S}\widetilde{\Delta G_v} + \widetilde{A_{S,L}}\widetilde{\gamma_{S,L}} + \widetilde{A_B}\widetilde{\Delta \gamma_{S-L,B}} + \widetilde{A_T}\widetilde{\Delta \gamma_{S-L,B}}. \tag{3.15}$$

Noting that $\widetilde{\Delta G_v} = 2$, $\widetilde{\gamma_{S,L}} = 1$, and $\widetilde{\Delta \gamma_{S-L,i}} = -cos(\theta_i)$,

$$\widetilde{\Delta G^{CL}} = -2\widetilde{V_S} + \widetilde{A_{S,L}} - \widetilde{A_B}cos(\theta_B) - \widetilde{A_T}cos(\theta_T). \tag{3.16}$$

In order to compute ΔG_c^{CL} using eqn. (3.16), the critical nucleus shape needs to be determined. The dimensionless shape of the nucleus is characterized by the function $\widetilde{y}(\widetilde{x})$, fig. 3.2. The nucleus shape is assumed to be the solid of revolution obtained by rotating $\widetilde{y}(\widetilde{x})$ about the $\widetilde{x}$ - axis. The dimensionless volume and areas terms are:

$$\widetilde{V_S} = \pi \int_0^{\widetilde{H}} (\widetilde{y}(\widetilde{x}))^2 \, d\widetilde{x}, \tag{3.17}$$

$$\widetilde{A_{S,L}} = 2\pi \int_0^{\widetilde{H}} \widetilde{y}(\widetilde{x}) \sqrt{1 + (\widetilde{y}'(\widetilde{x}))^2} d\widetilde{x}, \tag{3.18}$$

$$\widetilde{A_B} = \pi (\widetilde{y}_0)^2, \tag{3.19}$$

and

$$\widetilde{A_T} = \pi (\widetilde{y}_{\widetilde{H}})^2. \tag{3.20}$$
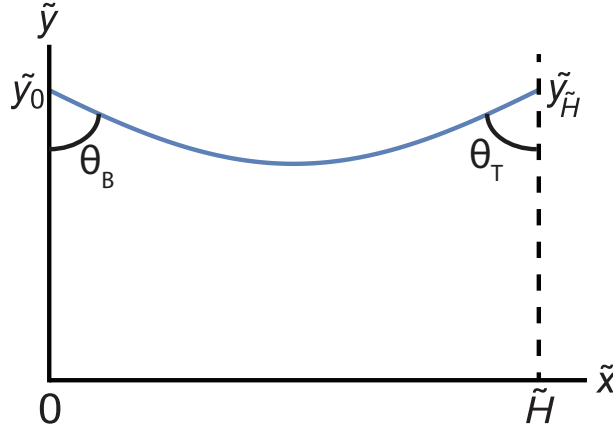
Figure 3.2: Illustration of CL nucleus represented by $\widetilde{y}(\widetilde{x})$. The CL nucleus is formed by revolving $\widetilde{y}(\widetilde{x})$ around the $\widetilde{x}$-axis.

The subscripts in $\widetilde{y}_0$ and $\widetilde{y}_{\widetilde{H}}$ refer to where $\widetilde{x}$ is being evaluated (fig. 3.2), and that notation will be used hereafter. These expressions are then substituted into eqn. (3.16), along with a volume constraint, by the use of a Lagrange multiplier, in order to determine the free energy function of the nucleus as a function of its volume.

$$\widetilde{\Delta G^{CL}}[\widetilde{x}, \widetilde{y}, \widetilde{y}'] = \int_0^{\widetilde{H}} (\lambda - 2) \pi (\widetilde{y}(\widetilde{x}))^2 + 2\pi \widetilde{y}(\widetilde{x}) \sqrt{1 + (\widetilde{y}'(\widetilde{x}))^2} d\widetilde{x}$$
$$- \pi (\widetilde{y}_0)^2 \cos(\theta_B) - \pi (\widetilde{y}_{\widetilde{H}})^2 \cos(\theta_T) \tag{3.21}$$

Minimizing $\widetilde{\Delta G^{CL}}$ yields the following second order differential equation for $\widetilde{y}(\widetilde{x})$

$$\sqrt{1 + \widetilde{y}'(\widetilde{x})^2} + \widetilde{y}(\widetilde{x}) \left((-2 + \lambda) \left(1 + \widetilde{y}'(\widetilde{x})^2\right) - \frac{\widetilde{y}''(\widetilde{x})}{\sqrt{1 + \widetilde{y}'(\widetilde{x})^2}} \right) = 0, \tag{3.22}$$

subject to the constraints $\widetilde{y}_0' = -cot(\theta_B)$ and $\widetilde{y}_{\widetilde{H}}' = cot(\theta_T)$. Note that these conditions ensure that the correct contact angles between the nucleus and the substrates are maintained. Solving eqn. (3.22) numerically using the shooting method with these boundary constraints allows the shape and dimensionless critical nucleation energy barrier to be determined. Due to the nature of the free energy versus volume function for this system, only one extrema exists. Thus, by setting $\lambda = 0$, the critical nucleation energy barrier for the CL nucleus can be directly determined. The nature of these free energy functions will be elaborated upon in the discussion section and for that analysis the Lagrange multiplier is used to vary the volume of the nucleus. Within the theory, there are three free parameters: θ_B, θ_T, and $\widetilde{H}$. At each point in the three dimensional space the nucleation energy barrier is calculated for both CL and cap nucleation, when applicable, and is compared. The morphology with the smallest nucleation energy barrier is considered to be the dominant form of nucleation for those parameters. The NMD displays this information by plotting the contiguous volumes representing the nucleus morphology with the smallest nucleation energy barrier.

3.3   Results

In this section the details of the NMD are discussed in the context of solidification, beginning with the case of $\theta_B = \theta_T$, and then generalizing to the case where θ_B does not necessarily equal θ_T. In order to understand the NMD, a brief discussion of $\widetilde{H}$ is required. As $\widetilde{H} = H/r_c$, the dimensionless height can be expressed in the following manner using eqn. (3.1) and eqn. (3.3).

$$\widetilde{H} \simeq \frac{H\Delta T \Delta H_v^F}{2T_M\gamma_{S,L}} \tag{3.23}$$

$\widetilde{H}$ contains, among other system parameters, the undercooling of the system, such that when $\widetilde{H}$ is positive (negative), the system's temperature is lower (higher) than the thermodynamic bulk melting temperature of the film, where the thermodynamic bulk melting temperature of the film is represented by $\widetilde{H} = 0$ for positive finite values of H. (At $T_M = T$, r_c diverges; however, since $\widetilde{H} = H/r_c$, as r_c diverges, $\widetilde{H}$ approaches 0.)

Nucleus Morphology Diagram: Symmetric Case

In fig. 3.3, three regions are present: cap nucleation, CL nucleation, and no nucleation. The cap and CL nucleation regions show the area of parameter space where each type of nucleation has the lowest critical nucleation energy barrier. In the no nucleation region, no nucleation of either type occurs. The boundary between the CL nucleation region and the no nucleation region is the film's constrained thermodynamic melting temperature. The critical nucleation energy barriers associated with fig. 3.3 are shown in fig. 3.4. The contour lines shows the direction of decreasing and increasing critical nucleation energy barriers as a

function of θ and $\widetilde{H}$. It should be noted that the critical nucleation energy barriers diverge as the parameters approach the no nucleation region.
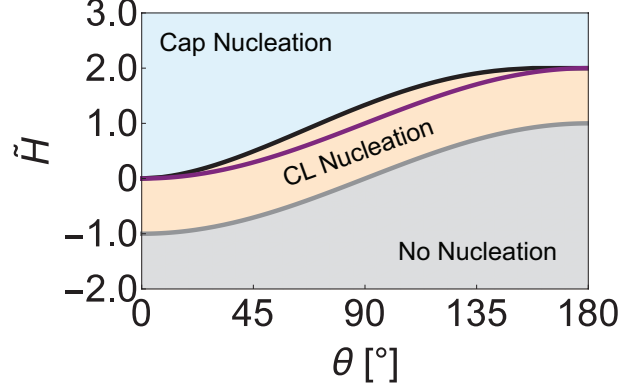

Figure 3.3: Slice of the NMD for the symmetric system, when the top and bottom substrate are the same, $\theta_B = \theta_T = \theta$. The cap and CL nucleation regions show the region of parameter space where each type of nucleation had the lowest critical nucleation energy barrier. In the third region, the no nucleation region, no nucleation of either type occurs. The grey curve is the boundary between the CL nucleation region and the no nucleation region, and is the film's constrained thermodynamic melting temperature. As $\widetilde{H} = 0$ represents the thermodynamic bulk melting temperature, the grey curve displays the conditions for the depression and elevation of the film's constrained melting temperature relative to the thermodynamic bulk melting temperature. The black curve is the cap and CL nucleation boundary, where the cap and CL structures have the same nucleation energy barrier. For a given contact angle, the purple curve signifies the minimum film thickness where a cap nucleus can attain its critical size.

The region in which no nucleation occurs can be determined using the following analysis. For the case where $\theta_B = \theta_T$, the volume of the CL nucleus scales as $\pi(\widetilde{y}_0)^2\widetilde{H}$, the solid-liquid surface area scales as $2\pi\widetilde{y}_0\widetilde{H}$, and the contact areas between the substrate and the nucleus for the top and bottom surfaces scale as $\pi(\widetilde{y}_0)^2$, as $\widetilde{y}_0 = \widetilde{y}_{\widetilde{H}}$. As the volume of the CL nucleus increases, the leading terms are the volume and the contact areas, as they scale as $(\widetilde{y}_0)^2$. It is a necessary thermodynamic condition that as the volume approaches infinity, and thus as $\widetilde{y}_0$ approaches infinity, $\widetilde{\Delta G^{CL}}$ must approach negative infinity, otherwise the system will not solidify. Thus for $\theta_B = \theta_T$ when $-cos(\theta) > \widetilde{H}$, the free energy of the system is not lowered by the creation and growth of the solid phase. Therefore $cos(\theta) = -\widetilde{H}$ represents the constrained thermodynamic melting temperature of the system. For the case where the top and bottom substrates are not the same, the contact area between the bottom surface and the nucleus still scale with $\pi(\widetilde{y}_0)^2$ whereas the contact area between the top surface and the nucleus scales as $\pi(\widetilde{y}_{\widetilde{H}})^2$. However, $\widetilde{y}_0$ and $\widetilde{y}_{\widetilde{H}}$ are of similar order, and thus if $cos(\theta_B) + cos(\theta_T) < -2\widetilde{H}$, nucleation does not occur, and the constrained thermodynamic melting temperature is defined by $cos(\theta_B) + cos(\theta_T) = -2\widetilde{H}$. Figure 3.3, shows under
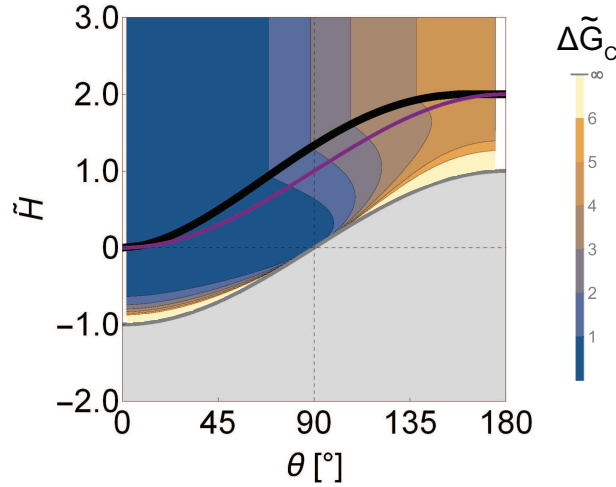
Figure 3.4: Critical nucleation energy barriers associated with the nucleation shown in 3.3. The black curve is the boundary between cap and CL nucleation and the purple curve signifies the minimum film thickness where a cap nucleus can attain its critical size. The grey curve is the film's constrained thermodynamic melting temperature. The plotted critical nucleation energy barriers range from $\theta = 2°$ to $\theta = 175°$.

what conditions the depression and elevation of the melting point are possible for $cos(\theta_B) = cos(\theta_T)$.

Nucleus Morphology Diagram

Figure 3.5 is the full NMD, showing a portion of the CL nucleation region and the full no nucleation region. The cap nucleation region is the part above the CL nucleation region, as the orange curve is the boundary between the CL and cap nucleation regions. Slices of constant $\widetilde{H}$ are shown in fig. 3.6, which show the different regions of the NMD for given values of $\widetilde{H}$.

Melting Temperature Shift

The border between the no nucleation and CL region in the NMD, indicates where the melting temperature is either depressed or elevated relative to the thermodynamic bulk melting temperature of the film's material. The maximum shift in the melting temperature can be approximated in terms of the materials parameters. Using eqn. (3.23) and eqn. (3.3), along with the conditions of no nucleation previously shown, the maximum elevation and depression of the melting temperature, ΔT, was determined for the symmetric and nonsymmetrical case:
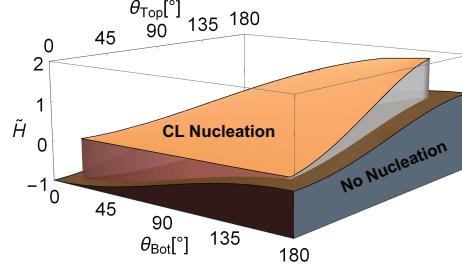
Figure 3.5: Full NMD showing the full no nucleation region and a portion of the CL nucleation region. The cap nucleation region is above the CL nucleation region, and the orange curve is the boundary between the CL and cap nucleation regions.
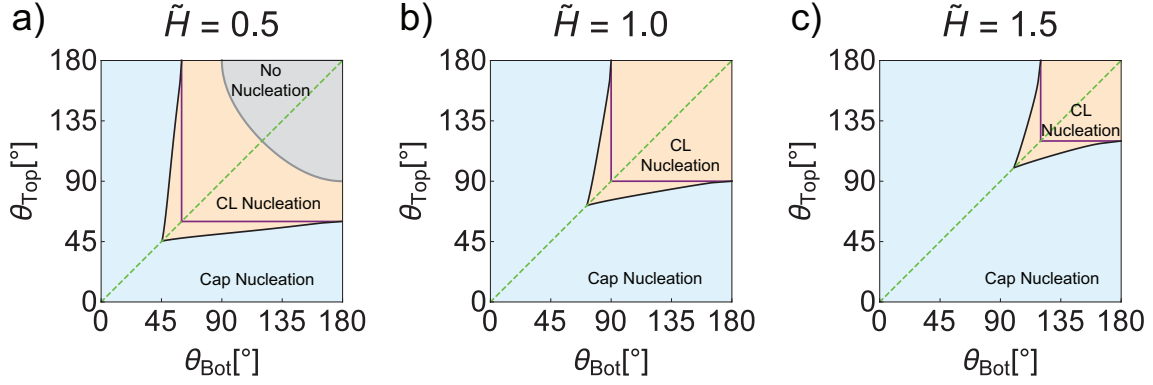
Figure 3.6: Slices of the full NMD with constant values of $\widetilde{H}$. (a) $\widetilde{H} = 0.5$, (b) $\widetilde{H} = 1.0$, (c) $\widetilde{H} = 1.5$. The cap and CL nucleation regions show the region of parameter space where each type of nucleation had the lowest critical nucleation energy barrier. In the third region, the no nucleation region, no nucleation of either type occurs. The grey curve is the boundary between the CL nucleation region and the no nucleation region, and is the film's constrained thermodynamic melting temperature. The black curve is the cap and CL nucleation boundary, where the cap and CL structures have the same nucleation energy barrier. For a given contact angle, the purple curve signifies the minimum film thickness such that the cap nucleus can attain its critical size. The dashed green line shows where the slice for the symmetric case, shown in fig. 3.3, is located on these figures, and illustrates the symmetry in the NMD, as there is nothing unique about θ_B and θ_T as expected.

$$\Delta T = -\frac{2T_M \gamma_{S,L} cos(\theta)}{H \Delta H_v^{Fus}}, \tag{3.24}$$

$$\Delta T = -\frac{T_M \gamma_{S,L}(cos(\theta_B) + cos(\theta_T))}{H \Delta H_v^{Fus}}. \tag{3.25}$$

Equation (3.24) was reported by Takagi [25] in 1986 and eqn. (3.25) reflects the situation where the top and bottom surfaces are not the same. For the symmetric system, when $90° < \theta \leq 180°$, ΔT in eqn. (3.24) is positive, whereas when $0° \leq \theta < 90°$, ΔT is negative. The former situation refers to a depression in the melting temperature, whereas the latter represents an elevation in the melting temperature. A similar effect is also evident for eqn. (3.25) depending on whether or not $(cos(\theta_B) + cos(\theta_T))$ is positive or negative.

3.4   Discussion

Melting Phase Transition and Nucleation Behavior

The same analysis can be performed for the melting phase transition. By redefining the contact angles to be between the liquid nucleus and the substrate, and changing the definition of ΔG_v to the difference between the solid phase from the liquid phase, which changes the definition of the critical radius, the same NMD found for solidification can be used for melting. This also changes the definition of ΔT to $\Delta T = T - T_M$ for eqns (3.3), (3.23), (3.24), and (3.25) and thus when reading figs. 3.3, 3.4, 3.5, and 3.6, note that when $\widetilde{H}$ is positive (negative), that refers to a temperature that is above (below) the thermodynamic bulk melting temperature. It is assumed that the same interface energy terms are applicable during solidification and melting, such that $\theta_{Solidification} + \theta_{Melting} = 180°$, and consequently the melting point shift is the same during solidification and melting, for a given set of system parameters, as expected. To summarize, when the top and bottom substrates are the same, denoted as substrate i, when $\widetilde{\gamma_{L,i}} > \widetilde{\gamma_{S,i}}$, there is an elevation of the melting temperature of the film, whereas when $\widetilde{\gamma_{S,i}} > \widetilde{\gamma_{L,i}}$, there is a depression of the melting temperature of the film. (Similar trends are found for the nonsymmetric case and can be found using eqn. 3.25.)

As evident by eqn. (3.24) and eqn. (3.25), materials with large values of $\frac{T_M \gamma_{S,L}}{\Delta H_v^{Fus}}$ have a greater potential to have their melting temperatures depressed or elevated, compared to a material with small values of $\frac{T_M \gamma_{S,L}}{\Delta H_v^{Fus}}$. Using interface energies determined by Turnbull [30], values of $\frac{T_M \gamma_{S,L}}{\Delta H_v^{Fus}}$ for the elements studied in Turnbull's work [30], are presented in table 3.1. Based upon the materials presented, transition metals such as Pt, Pd, and Fe, have a greater potential to have large elevations and depressions in their melting temperature.

In order to understand how geometric conditions and how substrate selection influence the nucleation behavior of confined thin films, the solidification and melting of Ge between two glass substrates is evaluated. The substrates are not specific to any one type of glass. Rather glass was chosen to reflect the conditions that epitaxy is not a part of the nucleation process being modeled, and that a wide range of glasses could be used to achieve the desired contact angle with the nuclei. Using $\gamma_{S,L} = 0.285 J/m^2$ [31, 32], $\widetilde{H}$ in terms of Ge parameters is the following.

Element	$\frac{T_M \gamma_{S,L}}{\Delta H_v^{Fus}}$ [nm K]
Ga	35.8
Hg	37.0
Bi	58.1
Sn	63.9
Pb	76.6
Al	81.1
Sb	84.2
Ge	94.1
Cu	130.1
Ag	141.6
Au	144.1
Ni	168.8
Co	169.1
Mn	174.4
Fe	189.9
Pd	202.5
Pt	222.8

Table 3.1: As a function of the elemental species, $\frac{T_M \gamma_{S,L}}{\Delta H_v^{Fus}}$, given in units of nm K, where the larger the value is, the greater potential to have large elevations and depressions in given material's melting temperature.

$$\widetilde{H_{Ge}} \simeq H \Delta T \frac{0.007}{nm\,K} \tag{3.26}$$

For example during the solidification of Ge, if the thickness of the thin film is 10 nm and the undercooling is 10 K, $\widetilde{H_{Ge}} \simeq 0.7$. Note that assuming the same interface energy terms are applicable during solidification and melting, such that $\theta_{Solidification} = 180° - \theta_{Melting}$, the critical nucleation energy barriers for melting and solidification of the same system are not necessarily the same, as seen in fig. 3.4. Therefore, an asymmetric hysteresis of the melting and solidification is expected when considering the thermodynamics and kinetics of nucleation. For instance, consider a 5 nm thick film of Ge between two identical glass substrates and assume that nucleation for both the solid and liquid phase can be approximated as occurring when $\widetilde{\Delta G_c} = 78 \widetilde{k_B T}$ [28]. From fig. 3.4 the temperatures at which nucleation of the solid phase occur during solidification and the liquid phase during melting can be estimated and are shown in fig. 3.7.

Figure 3.7 illustrates that there is an asymmetric hysteresis of nucleation for the solid and liquid phase around the film's thermodynamic melting temperature. Furthermore, relatively large supercooling and superheating effects are predicted [33]. For H = 5 nm the nucleation
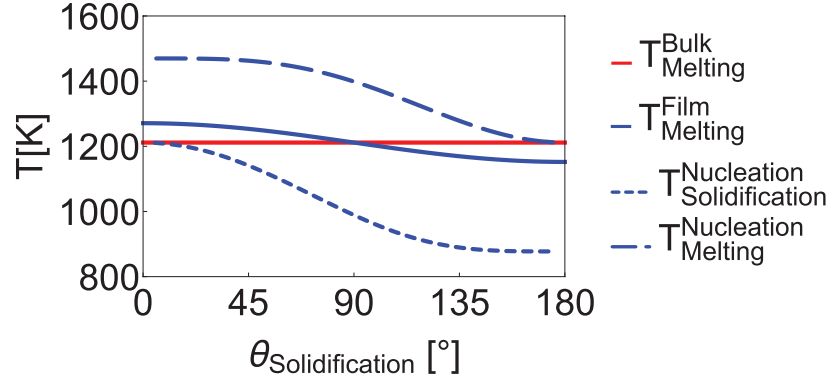
Figure 3.7: Nucleation temperature of the solid and liquid phase of Ge between two identical glass substrates, along with the Ge's thermodynamic bulk melting temperature, and the film's constrained thermodynamic melting temperature for H = 5 nm.

is mediated by cap nucleation. In order to study the hysteresis when CL nucleation is the predominate form of nucleation, the thickness of the film was reduced to 1.5 nm, and the hysteresis for that thickness is shown in fig. 3.8, again approximating that nucleation occurs for both phases when $\widetilde{\Delta G_c} = 78\widetilde{k_B T}$.
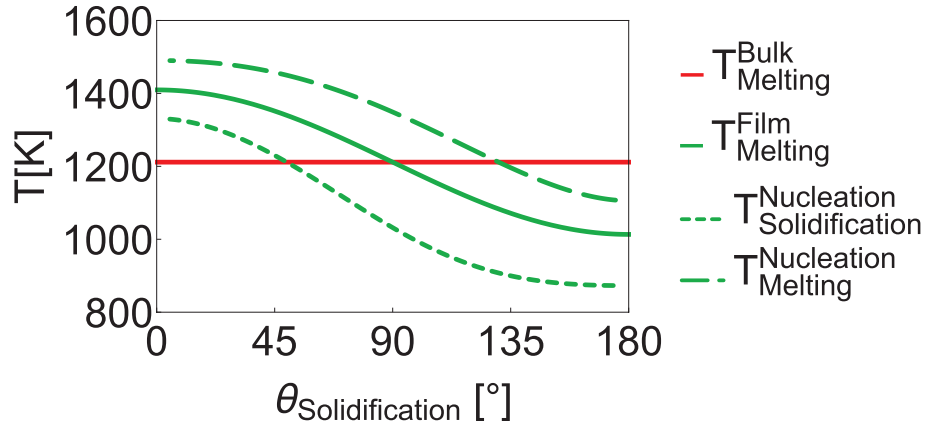
Figure 3.8: Nucleation temperature of the solid and liquid phase of Ge between two identical glass substrates along with Ge's thermodynamic bulk melting temperature, and the film's constrained thermodynamic melting temperature for H = 1.5 nm.

In fig. 3.8, it should be noted that relative to the bulk thermodynamic melting temperature, for $\theta_{Solidification} < 45°$ presolidification is predicted, and for $\theta_{Solidification} > 135°$ premelting is predicted. The difference between the nucleation temperature of the liquid phase and the nucleation temperature of the solid phase is plotted in fig. 3.9 for both H = 1.5 nm and H = 5 nm, and shows the widths of the hysteresis as a function of the solidification contact angle. The hysteresis of the constrained film is narrowed, relative to the

hysteresis for the thicker film. In both cases the maximum hysteresis is centered on the film's constrained thermodynamic melting point. The films display both superheating and supercooling.

Figure 3.9: Difference between the nucleation temperature of the liquid phase from the solid phase as a function of $\theta_{Solidification}$ for H = 1.5 nm and H = 5 nm.

Orientation Control

The theory also suggests a possible approach to achieving orientation control during the solidification of a confined film. Although an isotropic interface energy mode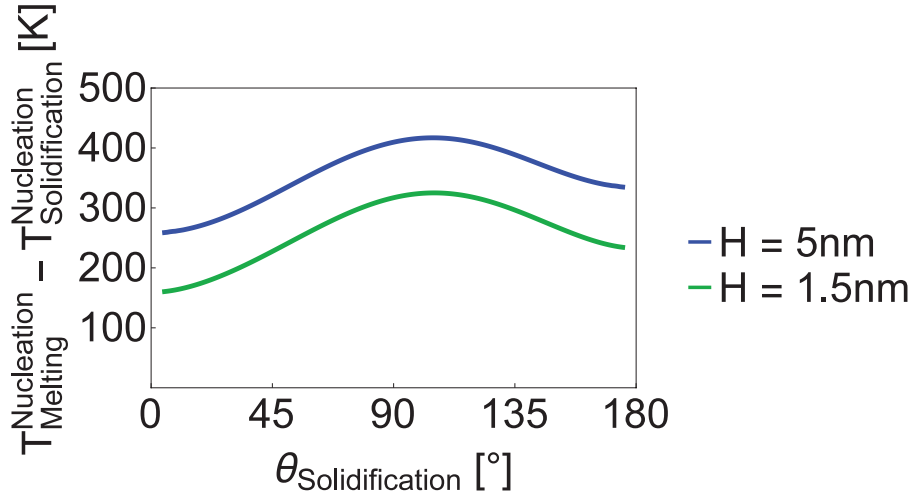l was used in the development of the theory herein, one can approximate the different film orientations relative to the substrate as having a different $\widetilde{\gamma_{S,i}}$. From the Young equation, differing $\widetilde{\gamma_{S,i}}$ lead to differing contact angles. From figs. 3.7 and 3.8 the temperature at which nucleation of the solid phase is predicted varies as a function of the contact angles. Thus, if the temperature is lowered to a value where some orientations are predicted to solidify and others are not, one might be able to prevent certain orientations from being grown. Experimentally, this may be achievable by lowering the annealing temperature within the range of the solidification temperatures and allowing nucleation to occur at that temperature before further cooling the system.

For the example system studied when H = 5 nm in fig. 3.7 the nucleation type is cap nucleation. As the thickness of the film increases, the nucleation type is still cap nucleation and consequently the nucleation temperatures will not change, as the critical nucleation energy barriers for cap nucleation are not thickness dependent. However, the nucleation temperatures when the nucleation type is CL do change depending on the thickness of the film. Additionally, the solid nucleation temperature has a greater range when the film's nucleation is occurring via CL nucleation. For the given examples, the solidification temperature range

is larger by a factor of approximately 1.37 for the H = 1.5 nm system compared to the H = 5 nm system. Therefore by confining the film to nucleate via CL nucleation, there is a greater chance of enhancing the ability to select certain orientations. Similar trends are also observed even if a different factor is used to equate $\widetilde{\Delta G_c}$ to $\widetilde{k_B T}$.

Trends found using the symmetric case can also be generalized to the nonsymmetric case. If one substrate is application specific but the other is not, selection of the other substrate can lead to various effects. During solidification for instance, if one is trying to depress the constrained thermodynamic melting temperature and the solidification nucleation temperature, it is typically advantageous to use a second substrate that has an equivalent or greater contact angle with a given nucleus. The smallest contact angle will typically dictate the nucleation behavior, and the critical nucleation energy barrier increases monotonically with increasing contact angles. Alternatively, if solidification at higher temperatures is desired, if the application specific material has a high contact angle with the nuclei, it would be advantageous to choose a second substrate the makes a smaller contact angle with the nuclei, due to the presolidification behavior found herein.

CL Nucleation Kinetic Pathway

Unlike the free energy versus volume function of the cap, the CL nuclei in general cannot start at zero volume. Rather, the CL nucleus must have a minimum volume, in most cases. (An exception to this is when $\theta_B = \theta_T = 90°$, as this system's geometry is a cylinder, and the free energy of this system can start at zero volume.) Therefore a kinetic pathway from zero volume to the CL solutions must be found. We explore transition paths for various contact angles and $\widetilde{H}$ values from the cap solution to the CL solution at a fixed volume. For the cases examined the energy never exceeds the CL energy at that volume.

The transition paths were found by solving the CL system with different heights, by incrementally increasing the height from the starting value defined by the cap to the $\widetilde{H}$ value under consideration. The system was solved using eqn. 3.22, and two boundary conditions. The first boundary condition is the slope of the curve in contact with the substrate, which is the contact angle of the nucleus, and this boundary condition remains fixed during the process. The second boundary condition is the slope of the curve at the point that is incrementally increased to $\widetilde{H}$. This slope was allowed to vary during the process. At each distance during the transition path, the boundary condition and the Lagrange multiplier were varied such that the lowest energy configuration for the given volume was found. It is possible to find transition paths where the boundary condition for the slope, at the end of the curve not in contact with the substrate, remains constant during the path. However, in general this is not true and the slope needs to be allowed to vary. Furthermore, if the slope is kept constant, and the energy during the path does not exceed the CL energy, this could be a viable path but there could exist a path that if the slope was allowed to vary, at each configuration a lower energy structure may exist. At the point that is incrementally increased for the transition path solutions, a disk-like interface is formed. That solid-liquid interface energy is included when calculating the free energy of the nuclei.
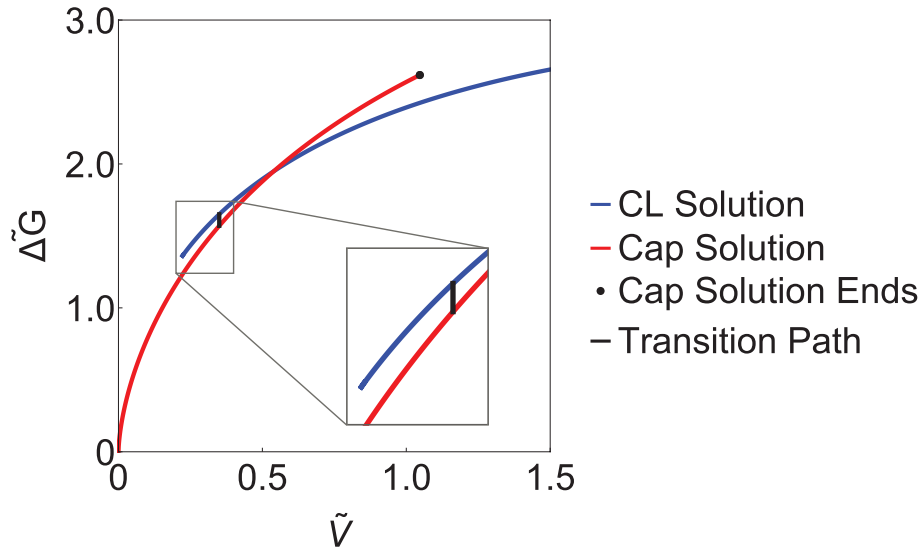
Figure 3.10: Dimensionless free energy versus volume for the CL and cap nucleus when $\theta_B = \theta_T = 120°$ and $\widetilde{H} = 1.0$. A transition path is shown from the cap solution to the CL solution.
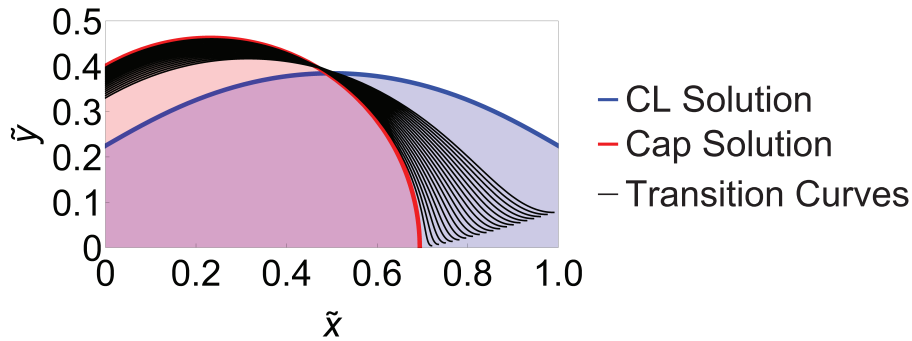
Figure 3.11: The $\widetilde{y}(\widetilde{x})$ curves representing the transition path from the cap solution to the CL solution for $\theta_B = \theta_T = 120°$ and $\widetilde{H} = 1.0$. For this transition path, which did not exceed the CL energy, the slope at the end point of the function was fixed to equal zero. The shape of cap nucleus, CL nucleus, and transition nuclei are created by rotating the solution around the $\widetilde{x}$-axis. The transition paths shown have a disk-like top at their end points, and that solid-liquid interface energy is included when calculating the free energy of the nuclei.

This process is by no means a proof that a transition path can always be found without an additional energy barrier at any volume. That study will be left to future research. Nonetheless, it does provide evidence that such a path is possible. An example of a transition path between the cap and CL free energy curves is shown in fig. 3.10 for the situation where

$\widetilde{H} = 1.0$ and $\theta_B = \theta_T = 120°$. The $\widetilde{y}(\widetilde{x})$ curves that represent the transition path shown in fig. 3.10, are displayed in fig. 3.11. For this situation a path is found where the slope of the free end of the $\widetilde{y}(\widetilde{x})$ function is fixed to zero.
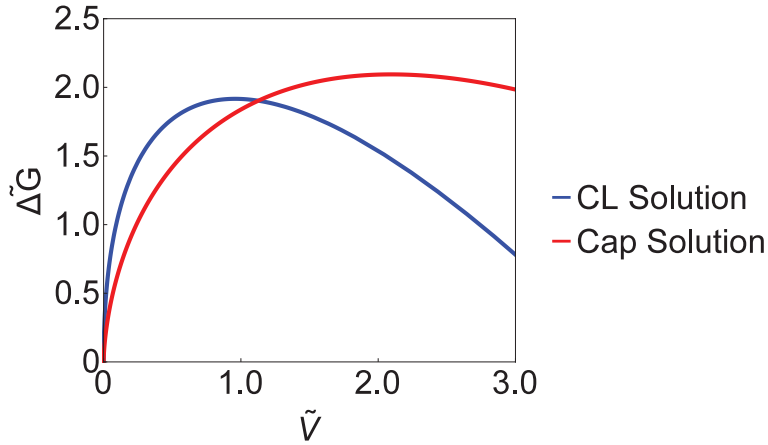
Figure 3.12: Dimensionless free energy versus volume for the CL and cap nucleus when $\theta_B = \theta_T = 90°$ and $\widetilde{H} = 1.22$. The CL solution is the predicted nucleation type, however, the system's smallest energy barrier may be given by the intersection of the two solutions.
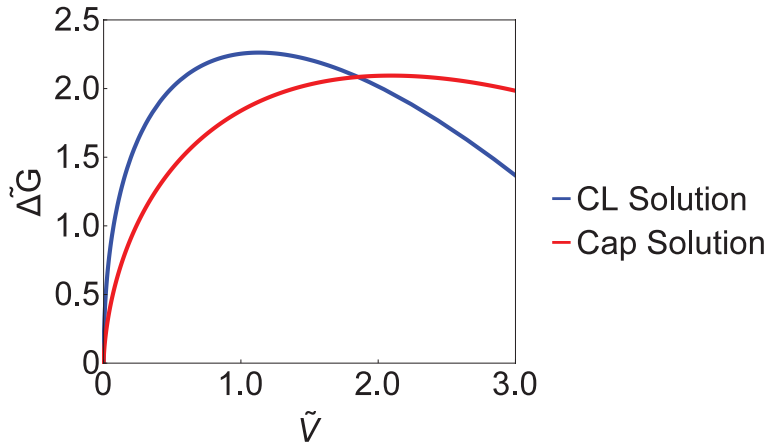
Figure 3.13: Dimensionless free energy versus volume for the CL and cap nucleus when $\theta_B = \theta_T = 90°$ and $\widetilde{H} = 1.44$. The cap solution is the predicted nucleation type, however, the system's smallest energy barrier may be given by the intersection of the two solutions.

If it is possible that there can be a transition path between the two nucleus solutions then the effective nucleation energy barrier could change at various locations in the NMD. If the transition can occur with no or relatively small transition barrier, the experimentally

observed nucleation energy barrier might be governed by the intersection of the two different free energy functions. Examples of this are shown in fig. 3.12 and in fig. 3.13.
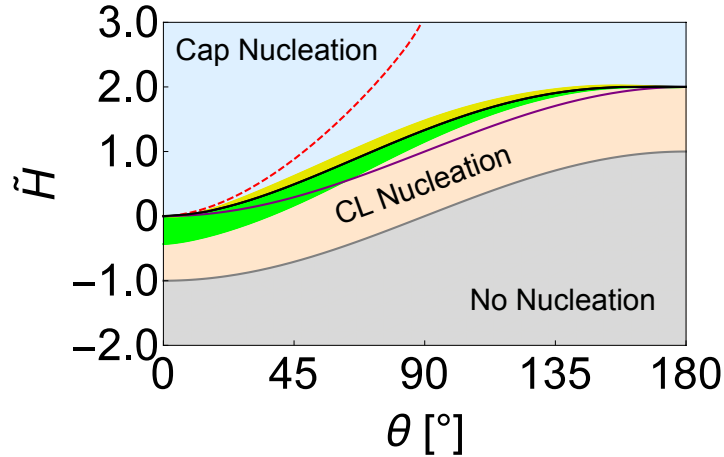

Figure 3.14: Symmetric slice of the NMD, where the regions and curves are the same as that in fig. 3.3, except for the discontinuous CL nucleation energy barrier curve (the dashed red curve) and regions A (green region) and B (yellow region). The discontinuous CL nucleation energy barrier curve is interpreted in the following way. For a given $\widetilde{H}$ value, the CL nucleation energy barrier at θ values between the curve and the $\widetilde{H}$-axis are discontinuous. Region A represents the case where the CL system has the smallest nucleation energy barrier, but the system's smallest energy barrier may be given by the intersection of the two free energy curves. Region B represents the locations where the cap system has the smallest nucleation energy barrier but the system's smallest energy barrier may be given by the intersection of the two free energy curves.

There are two main situations that can occur when considering the intersection point. First is the situation where the CL solution is the predicted nucleation type as it either has the lowest nucleation energy barrier or is the only nucleation type with a nucleation energy barrier. For this situation the actual nucleation energy barrier may be given by the intersection of the CL and cap free energy curves. In other words, by going from a volume of zero to a volume of infinity the path with the smallest barrier could be defined by starting on one free energy curve and then at the intersection point, switching to the other free energy curve. An example of this is shown in fig. 3.12, and is referred to as region A in fig. 3.14. The other situation that can occur is when cap solution is the predicted nucleation type, but the actual nucleation energy barrier may be given by the intersection of the two free energy curves. An example of this situation is shown in fig. 3.13, and is referred to as region B in fig. 3.14. Figure 3.14 shows the symmetric NMD with the addition of regions A and B. In these regions the actual nucleation energy barrier may be dictated by the intersection of the free energy curves.

Additionally, fig. 3.14 displays a curve that illustrates when a CL nucleation energy barrier is discontinuous. For $\widetilde{H}$ and θ values between the curve and the $\widetilde{H}$-axis, the CL system's nucleation energy barrier is discontinuous. Specifically, the maximum in the system's free energy curve as a function of volume is discontinuous. An example of this is shown in fig. 3.15. The physical reason why the CL system does not have a continuous nucleation energy barrier in this region, along with the viability of transitioning between free energy curves will also be a topic of future research.
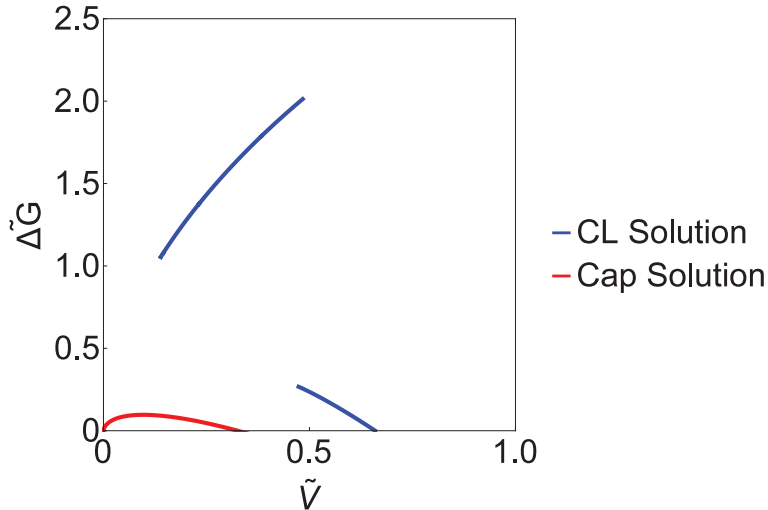

Figure 3.15: Dimensionless free energy versus volume for the CL and cap nucleus when $\theta_B = \theta_T = 35°$ and $\widetilde{H} = 1.0$. The free energy as a function of volume for the CL solution is discontinuous at its maximum.

Model Assumptions

Several assumptions were used to construct the model, and the justification and consequences of the primary assumptions are discussed. First, the volume change of the solid and liquid phase during the phase transition was neglected. Indeed the $P\Delta V$ contribution to the free energy due to the volume change upon a phase transition could be significant depending on the material being used in a confined thin film geometry. Nonetheless, the primary goal of this paper was to find overall trends of nucleation in confined thin films for nonepitaxial systems. This dissertation offers a framework to which additional effects, such as free energy changes associated with volumetric changes could be included.

The model used a continuum theory to describe phenomena on the nanometer length scale. Previous work by Q. Xu *et al.* [33] has shown that classical nucleation theory was successful in modeling systems of similar sizes. Specifically, classical nucleation theory was successfully used to model the melting temperature hysteresis of Ge nanoparticles during melting and solidification, where the nanoparticles had an average diameter of 5 nm [33],

thereby demonstrating that these theories can offer insight at small length scales. Next, the Gibbs free energy difference between the solid and liquid phases per unit volume was approximated by eqn. (3.3). This approximation is typically valid for small values of ΔT relative to the thermodynamic bulk melting temperature. Additionally, an isotropic interface energy model was used, and that assumption is typically only valid near the melting temperature. Some of the results shown reflect temperatures that are relatively far from the thermodynamic melting temperature. Nonetheless, the results presented are still valuable by showing trends of which materials and geometric conditions yield the greatest chance of influencing nucleation in a confined geometry. Therefore, this model offers a first approximation to the question of how nucleation is affected by confining a film in one dimension, and offers a possible route for orientation control in the studied geometry.

Chapter 4

Conclusion

The goal of this work was to present theories that can be used to achieve optimum growth characteristics for two material systems: nanoparticles embedded in a matrix and confined high-aspect ratio thin films. Based upon a mathematical argument, a previously proposed processing route for the synthesis of nanoparticles with a narrow size distribution during IBS has been explained using a self-consistent mean-field theory. By transitioning from a small SSAR to a larger SSAR the size distribution of nanoparticles can be narrowed substantially. One means of realizing these conditions is to ramp the temperature during implantation. Initial investigations suggest that widths of the size distributions can be reduced to less than 17 % of the average size. The theory thus serves as a useful guide for controlling size distributions during IBS.

Using classical nucleation theory, a nucleus morphology diagram was created for nucleation during the solidification and melting phase transitions for confined high aspect ratio thin films as a function of the thickness of the film and the system's bulk and interface energies. These diagrams show under what circumstances cap, CL, and no nucleation occur. Furthermore, expressions for the depression and elevation of the film's melting temperatures were found. Using these diagrams and expressions, experiments can be tuned to have greater control over the final microstructure of thin films. A new phenomena, termed presolidifcation, was identified. Additionally, although this model is based upon a single component system, the general trends found herein can be used as a first step in understanding the nucleation behavior of multicomponent systems, and offers a framework to which additional effects can be added to the model.

Bibliography

[1] V. D. Borman et al. "Evolution of the electronic properties of transition metal nanoclusters on graphite surface". In: *Journal of Experimental and Theoretical Physics* 110.6 (2010), pp. 1005–1025.

[2] R. H. Magruder III et al. "Optical properties of gold nanocluster composites formed by deep ion implantation in silica". In: *Applied Physics Letters* 62.15 (1993), pp. 1730–1732.

[3] Y. Yin and A. P. Alivisatos. "Colloidal nanocrystal synthesis and the organic-inorganic interface". In: *Nature* 437.7059 (2005), pp. 664–670.

[4] E. M. Chan et al. "Reproducible, High-Throughput Synthesis of Colloidal Nanocrystals for Optimization in Multidimensional Parameter Space". In: *Nano Letters* 10.5 (2010), pp. 1874–1885.

[5] A. M. Smith and S. Nie. "Semiconductor Nanocrystals: Structure, Properties, and Band Gap Engineering". In: *Accounts of Chemical Research* 43.2 (2010), pp. 190–200.

[6] P. Dimitrakis et al. "Silicon nanocrystal memory devices obtained by ultra-low-energy ion-beam synthesis". In: *Solid-State Electronics* 48.9 (2004), pp. 1511–1517.

[7] I. D. Sharp et al. "Stable, freestanding Ge nanocrystals". In: *Journal of Applied Physics* 97.12 (2005), p. 124316.

[8] C. W. Yuan et al. "Theory of Nanocluster Size Distributions from Ion Beam Synthesis". In: *Physical Review Letters* 102 (14 2009), p. 146101.

[9] L. Zhou et al. "Narrow size distribution of Au nanocrystals formed in sapphire by utilizing Ar ion irradiation and thermal annealing". In: *Nuclear Instruments and Methods in Physics Research Section B: Beam Interactions with Materials and Atoms* 278 (2012), pp. 42–45.

[10] Y. Ramjauny et al. "Controlling the size distribution of embedded Au nanoparticles using ion irradiation". In: *Journal of Applied Physics* 107.10 (2010), p. 104303.

[11] V. Ramaswamy et al. "Synthesis of Nearly Monodisperse Embedded Nanoparticles by Separating Nucleation and Growth in Ion Implantation". In: *Nano Letters* 5.2 (2005), pp. 373–377.

[12] C. W. Yuan et al. "Processing route for size distribution narrowing of ion beam synthesized nanoclusters". In: *Applied Physics Letters* 95.8 (2009), p. 083120.

[13] C. W. Yuan et al. "Size-distribution evolution of ion-beam-synthesized nanoclusters in silica". In: *Physical Review B* 80 (13 2009), p. 134121.

[14] D. O. Yi et al. "Modeling nucleation and growth of encapsulated nanocrystals: Kinetic Monte Carlo simulations and rate theory". In: *Physical Review B* 78 (24 2008), p. 245415.

[15] C. W. Yuan. "Modeling size distribution evolution of ion-beam-synthesized nanoclusters in amorphous silica". PhD thesis. University of California, Berkeley, 2009.

[16] J. A. Marqusee and J. Ross. "Theory of Ostwald ripening: Competitive growth and its dependence on volume fraction". In: *The Journal of Chemical Physics* 80.1 (1984), pp. 536–543.

[17] L. Ratke and P. W. Voorhees. *Growth and Coarsening*. 1st ed. Verlag, Germany: Springer, 2002.

[18] R. Kissel and H. M. Urbassek. "Sputtering from spherical Au clusters by energetic atom bombardment". In: *Nuclear Instruments and Methods in Physics Research Section B: Beam Interactions with Materials and Atoms* 180.1-4 (2001), pp. 293–298.

[19] S. Hu et al. "Single-crystal germanium layers grown on silicon by nanowire seeding". In: *Nature Nanotechnology* 4 (10 2009), pp. 649–653.

[20] R. Kapadia et al. "A direct thin-film path towards low-cost large-area III-V photovoltaics". In: *Scientific Reports* 3 (2013), p. 2275.

[21] R. Kapadia et al. "Deterministic Nucleation of InP on Metal Foils with the Thin-Film Vapor-Liquid-Solid Growth Mode". In: *Chemistry of Materials* 26 (2014), pp. 1340–1344.

[22] K. Chen et al. "Direct growth of single-crystalline III-V semiconductors on amorphous substrates". In: *Nature Communications* 7 (2016), p. 10502.

[23] M. Takagi. "Electron-Diffraction Study of Liquid-Solid Transition of Thin Metal Films". In: *Journal of the Physical Society of Japan* 9 (1954), pp. 359–363.

[24] Q. Jiang et al. "Thermal stability of crystalline thin films". In: *Thin Solid Films* 312.1 (1998), pp. 357–361.

[25] M. Takagi. "The Thickness Dependence of the Phase Transition Temperature in Thin Solid Films". In: *Journal of the Physical Society of Japan* 55 (1986), p. 3484.

[26] L. Zhang et al. "Superheating of Confined Pb Thin Films". In: *Physical Review Letters* 85 (7 2000), pp. 1484–1487.

[27] D. Turnbull. "Phase Changes". In: *Solid State Physics* 3 (1956), pp. 225–306.

[28] D. A. Porter, K. E. Easterling, and M. Sherif. *Phase Transformations in Metals and Alloys, Third Edition*. 3rd ed. Boca Raton, FL: CRC Press, 2009.

[29]   I. M. Gelfand and S. V. Fomin. *Calculus of Variations*. 1st ed. USA: Dover, 2000.

[30]   D. Turnbull. "Formation of Crystal Nuclei in Liquid Metals". In: *Journal of Applied Physics* 21 (1950), pp. 1022–1028.

[31]   F. Caupin. "Comment on "Large Melting-Point Hysteresis of Ge Nanocrystals Embedded in SiO$_2$"". In: *Physical Review Letters* 99 (7 2007), p. 079601.

[32]   Q. Xu et al. "Xu et al. Reply". In: *Physical Review Letters* 99 (7 2007), p. 079602.

[33]   Q. Xu et al. "Large Melting-Point Hysteresis of Ge Nanocrystals Embedded in SiO$_2$". In: *Physical Review Letters* 97 (15 2006), p. 155701.